Investigation of Cu-Mn catalytic ozonation of toluene: Crystal phase, intermediates and mechanism.

Zhiping Ye, Guanjie Wang, Jean-Marc Giraudon, Anton Nikiforov, Jun Chen, Liang Zhao, Xiuwen Zhang, Jiade Wang

▶ **To cite this version:**

HAL Id: hal-04125432
https://hal.univ-lille.fr/hal-04125432

Submitted on 23 Oct 2023

Investigation of Cu-Mn catalytic ozonation of toluene: Crystal phase, intermediates and mechanism

Zhiping Ye [a], Guanjie Wang [a], Jean-marc Giraudon [b], Anton Nikiforov [c], Jun Chen [d], Liang Zhao [a], Xiuwen Zhang [a], Jiade Wang [a]*

[a] College of Environmental, Zhejiang University of Technology, 18 Chaowang RD, Xiacheng District, Hangzhou, China
[b] Univ. Lille, CNRS, Centrale Lille, ENSCL, Univ. Artois, UMR 8181-UCSS-Unité de Catalyse et Chimie du Solide, F-5900 Lille, France
[c] Ghent University, Faculty of Engineering, Department of Applied Physics, Research Unit Plasma Technology, Sint-Pietersnieuwstraat 41, 9000 Ghent, Belgium
[d] Interdisciplinary Research Academy, Zhejiang Shuren University, Hangzhou, 310021, P.R. China

*Corresponding Author

E-mail: jdwang@zjut.edu.cn

Abstract

The effect of different crystal phases, i.e. spinel phase ($CuMn_2O_4$) and amorphous phase ($Cu_{0.2}MnO_x$), was explored in Cu-Mn catalytic ozonation of toluene. The toluene removal efficiency followed the order of $Cu_{0.2}MnO_x$ (91.2%) > $CuMn_2O_4$ (74.5%) > commercial catalyst $Cu_{0.3}MnO_x$ (70.3%) in 130 min, and the higher CO_2 yield (67.6%) could be also observed using $Cu_{0.2}MnO_x$. In order to investigate the effect of phases on the toluene degradation pathway, the intermediates and byproducts were identified by DRIFTS, GC-MS, and TOF-SIMS. No obvious difference was observed in the distribution of byproducts, except for the quantities, suggesting the discrepancy of oxidation rate. On the other hand, the catalysts were characterized before and after the ozonation process by TEM, BET, XPS, XRD, EPR, TGA, and TPR. It was proposed that for amorphous catalysts, the oxygen vacancy (Vo) helped the chemisorption of toluene, and adjacent Mn reacted as the main active site for the ozonation process. While, the redox pair of Cu^+/Mn^{4+} and $Cu^{2+}/(Mn^{3+}, Mn^{2+})$ in the spinel phase plays an important role in the generation of oxygen vacancies for O_3 decomposition.

Keywords: Cu-Mn bimetallic oxide; Crystal phase; Catalytic ozonation; Reaction mechanism; Degradation pathway

1. Introduction

Volatile organic pollutants (VOCs) are the key precursors for urban photochemical smog, ozone (O_3), and atmospheric PM2.5, resulting in air pollution problems [1-3]. Therefore, VOCs abatement technologies have been widely studied. Among them, catalytic ozonation is recognized as an effective method for the low-temperature removal of VOCs [4, 5]. The removal efficiency has been highly investigated [6, 7]. The experimental parameters, such as humidity [6], temperature [8] and O_3 concentration [9], etc, have been regards as important factors. In addition, the selection of catalyst was also important for the ozonation process. MnO_x [10-14] is one of the popular catalysts used in catalytic ozonation of VOCs due to its outstanding performance in the abatement of VOCs and O_3. The performance of catalytic ozonation could be further improved when other metals are added into

MnO_x, such as Cu [15], Ce [16], etc. Jing Liu et al. [15] synthesized a series of copper doped manganese oxide octahedral molecular sieves (Cu-OMSx-T) with different Cu/Mn ratios and reported the best ratios of Cu/Mn was 0.5, and the improved performance was considered to be the synergistic effect between Cu and Mn ($Cu^{2+} + Mn^{3+} \rightleftharpoons Cu^+ + Mn^{4+}$) [14]. Considering the wide application of Cu-Mn oxides in catalytic ozonation of VOCs, it is worth further investigating the mechanism of the ozonation process, especially the effect of different Cu-Mn crystal phases.

Generally, the ozonation process over catalysts surface includes the adsorption of pollutant and O_3, ozone activation to generate reactive oxygen species (O^-, O_2^-, O_2^{2-}) for VOCs oxidation, and oxidation process [17]. The characteristic of catalysts plays an important role in the above-mentioned process, especially the different phases of catalyst [18, 19]. The different phases of Cu-Mn oxides can be controlled through various preparation methods, exhibiting different catalytic oxidation performances [20]. It is observed the well-distributed active sites of Cu-Mn and better redox properties using the amorphous sample resulting in excellent catalytic reactivity [21]. Chi-Woong Ahn et al. [22] found that the transformation of the catalyst crystal phase (from amorphous to crystalline phase) could strongly reduce the catalytic activity of the catalyst. Hong Chen et al. [23] synthesized amorphous Cu-Mn catalysts and reported good catalytic activity owing to the coexistence between crystallized CuO phase and amorphous Cu-Mn-O. Yu Wang et al. [24] reported that the interfacial structure of mixed phases (CuO and MnxOy) can induce the formation of Cu^{2+}-O^{2-}-Mn^{4+}, as well as improved the reducibility. However, the effects of various crystal and morphologies on catalytic ozonation of VOC are still unclear, especially the degradation pathway and the synergetic effect of Cu and Mn in the different crystal phases.

Hence, in this paper, the samples with spinel and amorphous phases were prepared, respectively, and they are compared to a commercial amorphous Cu-Mn sample ($Cu_{0.3}MnO_x$) in catalytic ozonation of toluene. The performances were evaluated by toluene conversion, CO_2 yield, CO yield, byproduct composition, and O_3 abatement. The corresponding toluene degradation pathway was studied using DRIFTS, GC-MS. In addition, in order to analyze the role of the crystal phase during the reaction, the fresh and the used catalysts were characterized through SEM, BET, XRD, TPR, EPR, TOF-SIMS, TGA, and XPS.

2. Experiment

2.1 Catalyst preparation

The $Cu_{0.2}MnO_x$ and $CuMn_2O_4$ catalysts were prepared by redox and co-precipitation methods, respectively. The detailed preparation process was described in our previous work [20]. The commercial catalyst was bought from Jining Yongbang Machinery Co. LTD and denoted as $Cu_{0.3}MnO_x$.

2.2. Catalyst characterization

The special surface area of the catalyst was determined according to the nitrogen adsorption and desorption isotherm, which is measured at -196℃ on a Micromeretics ASAP 2460 instrument after 5 h of venting at 200℃. The pore size distribution was determined using the Barrett-Joyner-Halenda (BJH) method.

X-ray diffraction (XRD) analysis of all catalysts was performed on PNAlytical X'Pert PRO powder diffractometer using the Cu Kα radiation at 40 kV and 40 mA. The 2θ angle ranged from 10° to 80° with a step of 0.0167°.

The morphologies of catalysts were detected by scanning electron microscopy (SEM) images and high resolution transmission electron microscope (HRTEM) images recorded on a Hitachi S-4700 apparatus (Ⅱ) and FEI Tecnai F30.

Inductively coupled plasma-optical emission spectroscopy (ICP-OES) was performed to obtain the metal elemental analysis of the samples (Cu and Mn) with the Agilent 720ES.

Electron paramagnetic resonance (EPR) experiments were performed with Bruker EMXPLUS (Germany).

Hydrogen temperature-programmed reduction (H2-TPR) was carried on the Chemisorb 2920 chemical adsorption analyzer (Micromeritics, USA). The catalysts were pretreated by pure He flows at 150℃ (30 ml/min) for 1 h, and then heated with a rate of 5℃/min up to 500℃ by using 5 vol.% H_2/Ar (50 ml/min) flow.

Thermogravimetric analysis and differential thermal analysis (TGA/DTA) were performed using the dried catalysts at a heating rate of 10℃/min up to 790℃ with the use of Discovery TGA 5500.

X-ray photoelectron spectroscopy (XPS) was recorded with Thermo Scientific K-Alpha. The binding energies (BE) were calibrated using the peaks of C 1s at 284.8 eV. Peak fitting was processed with CasaXPS.

Gas chromatography-mass spectrometer (GC-MS) was used to identify the by-products on the Agilent 7890A-5975C instrument, which is equipped with a DB-5MS column.

Time of flight secondary ion mass spectrometry (TOF-SIMS) was carried out to analyze the surface composition of the sample with TOF·SIMS5 spectrometer (ION-TOF GmbH Germany) using 30 keV Bi^{3+} primary ions (pulsed current 0.1 pA).

The diffuse reflectance infrared Fourier transform spectroscopy (DRIFTS) was applied to detect the changes of functional groups on the surface of catalysts during the reaction. The instruments used in the experiment were Nicolet IS50 FTIR and Harrick *in situ* reaction chamber (HVC-DRM) of Thermo Fisher Company. The scanning time was set to 256 scans and the resolution was 8 cm^{-1}.

2.3. Catalytic activity evaluation

The toluene catalytic performance of the sample was evaluated in a fixed bed flow continuous reactor at atmospheric pressure. The schematic diagram of the experimental setup is shown in Fig. S1. About 200 mg of samples (40-60 mesh) was loaded in the quartz reactor (i.d. = 8 mm) and fixed in position with quartz wool on both ends of the catalyst. The simulated reaction gas contains ~160 ppm toluene introduced by micro-injector, O_3, and dry air. The flow rate and O3 concentration were adjusted by mass flow controllers (MFC) and fixed at 700 ml/min and 2100 ppm, respectively. The performance was evaluated at 100℃ for 130 min. The concentration of toluene, CO, and CO_2 in outlet gas were detected by online gas chromatography (GC-9790H Fuli Gas Chromatography) equipped with thermal conductivity detector (TCD) and flame ionization detector (FID), and the columns of Restek Shin Carbon ST/Silco, HP NOC 80/100 micro-packed and capillary column Cp-Wax 52 CB25 m, Ø¼ 0.25 mm were installed. Toluene removal rate (TRR), CO yield (XCO) and CO2 yield (XCO2), and others (XO) were calculated in supporting information.

3. Results and Discussions

3.1. Characterization of samples

Cu0.2MnOx and CuMn2O4 catalysts were successfully synthesized (Fig. S2), and the corresponding catalyst characterization was in agreement with our previous report [20], exhibiting the phase of spinel CuMn2O4 and amorphous phase of Cu0.2MnOx. In order to further reveal the ozonation process of amorphous catalyst, a commercial catalyst was chosen with amorphous phase for comparison. As for Cu0.3MnOx, it was observed that the two wide diffraction peaks located in the 2 theta regions of 34-39° and 62-71°, indicating that they were essentially amorphous. The X-ray diffraction patterns of Cu0.2MnOx and Cu0.3MnOx have been plotted against temperature and presented in Fig. S3. As shown in Fig. S3, both materials heated in N_2 up to 400℃ still remained amorphous. For Cu0.2MnOx (Fig. S4),

it is revealed that a predominant phase of Mn_3O_4 and a minor phase of spinel $Cu_xMn_{3-x}O_4$ can be observed when temperature heated up to 500°C, and the additional peak of $CuMnO_2$ oxide (crednerite) can be found from 600 to 800°C. While, XRD of $Cu_{0.3}MnO_x$ showed that $CuMn_2O_4$ (PDF 34-1400) spinel oxide was formed and kept thermally stable in that temperature range of 500 to 800°C. The amorphous structure promotes the occurrence of lattice defects and the exposure of internal atoms, thus increasing the surface area of the catalyst [25], as seen in Table 1, the surface area of $Cu_{0.2}MnOx$ (154.3 m^2/g) and $Cu_{0.3}MnO_x$ (156.3 m^2/g) are much larger than spinel structure of $CuMn_2O_4$ (61.4 m^2/g).

The morphologies of catalysts were investigated by SEM and HRTEM. $Cu_{0.2}MnO_x$ and $CuMn_2O_4$ both show a similar morphology that aggregates nano-particles to form bigger particles. $CuMn_2O_4$ has particle size in the range of 20-40 nm, while, $Cu_{0.2}MnO_x$ sample exhibits smaller size of spherical particles in the range of 8-15 nm, and the $Cu_{0.3}MnO_x$ sample shows the surface morphology of a rod shape with the length of ~360 nm. The inset in Fig. 1A2, B2, C2 shows the selected area electron diffraction (SAED) pattern, and the morphologies of catalysts exhibit a polycrystalline structure in all samples. Furthermore, as shown in Fig. 1A3, it can be seen that there are interplanar spacing of 0.305 and 0.159 nm in $CuMn_2O_4$, corresponding to 220, 511 crystal planes, respectively, and the angle of the 220 and 511 crystal planes are 35°. The fast Fourier transform (FFT) index of $CuMn_2O_4$ was [1,1,-4] zone axis, indicating the crystal plane of {-114} was selectively exposed. Comparing to amorphous samples, regular and smooth lattice fringes of $CuMn_2O_4$ suggested a good crystallization as expected. On the other hand, it can be observed that sporadic crystals are randomly distributed on the "amorphous" matrix (highlighted by dark yellow ovals) for $Cu_{0.2}MnO_x$. It was proposed the lattice fringes are covered by a large number of point defects [26], and these defects were believed to be the oxygen vacancies. It is reported that the oxygen vacancy normally is located in the second layer of catalyst crystal structure [32]. Therefore, when oxygen defect exists in the structure, the adjacent metal atom will permeate to the defect location, resulting in a shaded region, and the shaded region was referred to as oxygen vacancy on the catalyst's surface as seen in blue ovals in Fig. S5. As for the existence of sporadic crystal domains, the minimum lattice spacing of $Cu_{0.2}MnO_x$ and $Cu_{0.3}MnO_x$ is 0.162 nm and 0.185 nm, respectively.

The information of chemical composition was investigated using XPS, the relevant results were illustrated in Fig. 2 and Table 1. Cu 2p XPS spectra were characterized by two distinct regions of 947-957 eV and 930-938 eV that corresponding to Cu $2p_{1/2}$ and Cu $2p_{3/2}$ spin orbitals, respectively. The peaks at 930.6 and 950.5 eV can be attributed to Cu^+. The signal at 933.4 and 953.2 eV accompanying with two shake-up satellites (S1 and S2) is Cu^{2+} [20]. Note that Cu^+ was detected only on the surface of $CuMn_2O_4$. The spectrum of Mn 2p can be deconvoluted into 6 peaks. The peaks located at 641.1 and 652.5 eV were referred to Mn^{3+}, and the signal at 639.7 and 647.5 eV were indicative of Mn^{2+} [27], whereas the Mn 2p signals at 643.0 and 655.8 eV were for Mn^{4+} [28]. The average oxidation state of Mn (Mn AOS) was calculated by the binding energy (ΔE) difference between the two peaks in Mn 3s (Mn AOS = 8.956 - 1.126 × ΔE) [29]. The results showed that the order of Mn AOS was $CuMn_2O^4$ (3.8) > $Cu_{0.3}MnO_x$ (3.6) > $Cu_{0.2}MnO_x$ (3.5), which indicates the possible form of Mn^{3+} or/and Mn^{2+} in samples, and the content of Mn^{4+} was higher in the spinel sample comparing to amorphous samples. Moreover, it was reported the bonds of Mn^{2+}-O and Mn^{3+}-O are weaker than Mn^{4+}-O [18], and more existence of low-valence Mn can weaken the Mn-O bond on the surface of the sample promoting the dissociation and activation of surrounding oxygen atoms. The atomic Cu/Mn ratio of $CuMn_2O_4$, $Cu0._2MnO_x$, and $Cu_{0.3}MnO_x$ from the results of energy dispersive X-ray spectroscopy (EDX) was 0.5, 0.6 and 2.1 comparing to 0.5, 0.2 and 0.3 from ICP-OES results, respectively, revealing more Mn on the amorphous catalysts surface.

The O 1s spectra can be deconvoluted into four peaks, corresponding to surface lattice oxygen (Olat, 529.8 eV), adsorbed oxygen (O_ads, 531.2 eV), vacancy oxygen (Ov,532.2 eV), and surface hydroxyl

oxygen (Sur-OH, 532.8 eV), respectively [30, 31]. Notably, the O_{lat} mainly plays an oxidizing role in the O_3 catalytic process, and is usually supplemented by the following path: O_3 (O^-, O_2^-, O_2^{2-}) + Ov $\rightarrow$ O_{ads} $\rightarrow$ O_{lat} [33]. Therefore, as shown in Fig. 3, a good performance of $Cu_{0.2}MnO_x$ could be achieved due to a higher O_{ads}/O_{lat} (0.8). The O_{ads}/O_{lat} of $CuMn_2O_4$ and $Cu_{0.3}MnO_x$ is 0.7 and 0.6, respectively.

The unpaired electrons in the samples were detected by EPR. As shown in Fig. 4, the signal of g value from the amorphous sample ($Cu_{0.2}MnO_x$ and $Cu_{0.3}MnO_x$) presents a slight reduction compared to that of the $CuMn_2O_4$ (1.9987). The results indicate that the enhancement of the electron density on the amorphous sample interface, contributing to the numerous lattice boundaries accompany with more oxygen vacancy [34]. It is expected that the electron-rich environment and the existence of more oxygen vacancies can effectively supplement the electron consumption of samples during catalytic ozonation.

Fig. 5 exhibits the samples of H_2-TPR profiles. Two reduction peaks can be observed for each sample on the profiles, suggesting a continuous reduction of Cu-Mn cations. $Cu_{0.2}MnO_x$ and $CuMn_2O_4$ show the first peaks of hydrogen consumption at 227℃ and 229℃, respectively, which are lower than that (252℃) of $Cu_{0.3}MnO_x$. This suggests the redox reactions of homemade catalysts at low temperatures are more active than the commercial catalyst. The continuous peaks were thought to be the reduction of the mixed-valence state of the Cu-Mn oxides, and the existence of Mn_xO_y also can prevent the reduction by forming a relatively stable $_{MnOx}$, resulting in the tailing peaks [35].

3.2. Catalytic ozonation of toluene

The toluene removal efficiency of three catalysts in 130 min as shown in Fig. 3A, exhibiting the order as follows: $Cu_{0.2}MnO_x$ (91.2%) > $CuMn_2O_4$ (74.5%) > $Cu_{0.3}MnO_x$ (70.3%). No obvious decrease in toluene removal efficiency was observed using all samples. Meanwhile, as Fig. 3B shown, better performances of O_3 decomposition at 100 ℃ were observed using homemade catalysts, while, for $Cu_{0.3}MnO_x$, O_3 concentration decreased to zero at the beginning, and then bounced back to ~400 ppm. It seems that the low temperature limits the O_3 decomposition of $Cu_{0.3}MnO_x$, leading to low toluene abatement. In order to confirm the role of O_3, the degradation of toluene was conducted without O_3 as shown in Fig. S6. Toluene removal efficiency vibrated at ~3%, and no obvious CO_2 was revealed in experiments. This suggested the O_3 was vital in toluene abatement as reported [36]. According to an overview table containing Cu or Mn-based ozonation of toluene in Table S1, the higher O_3 abatement was observed in our work, and the toluene removal efficiency is comparable to other works at ~100℃. Furthermore, based on the result of carbon balance in 130 min, the higher CO_2 yield was observed using $Cu_{0.2}MnO_x$, and the yield of CO_x (CO_2 + CO) was higher than 80%. For the spinel $CuMn_2O_4$, CO_2 yield was lower than that of amorphous samples, and it was revealed that ~ 17.7% of toluene turned into organic carbonaceous by-products.

3.3. The analysis of toluene decomposition

The toluene degradation pathway was explored through the technologies of GC-MS, DRIFTS, and TOF-SIMS. The results were displayed in Fig. 6-8 and Table S2. As shown in Fig. 6, a series of typical by-products (such as benzyl alcohol, benzaldehyde, benzoic acid, and maleic anhydride) were produced during the catalytic ozonation of toluene as reported [11, 37]. Note that other byproducts can be sorted into two types: benzenoids and ring-opening organic compounds (Table S3). It was revealed that the IR band at 1654 cm^{-1} was presented, which was assigned to the C=O stretching vibration of quinone compounds, the results in GC-MS spectra also confirmed the presence of O-methyl benzoquinone. The possible reaction route ③ was proposed as shown in Fig. 8 (C_7H_8 $\rightarrow$ C_6H_4 (CH_3)-OH $\rightarrow$ HO-C_6H_3(CH_3)-OH $\rightarrow$ O=C_6H_3(CH_3)=O) [11]. The strong peaks of 1450 and 1555 cm^{-1} were assigned

to the antisymmetric and symmetrical stretching vibration of COO-. The peaks at 1410, 1498, and 1600 cm^{-1} were considered to be in-plane skeletal vibrations of the aromatic ring, hence, the typical vibrations of aromatic ring and COO- were ascribed to the typical peaks of benzoic acid. Note that the COO- vibration of benzoic acid for home-made catalysts was much weaker than that with the use of $Cu_{0.3}MnO_x$, and it was observed the COO- peaks of $Cu_{0.3}MnO_x$ sample weakened after 5 min reactions. Moreover, the C-OH stretching vibration of alcohols (1039 cm^{-1}) was discovered for all samples, indicating the presence of phenyl methanol. The above discussed byproducts were also confirmed by GC-MS results. Note that propanol was found in GC-MS spectra, which may be further oxidized to propionic acid [38] as Eq. 1.1-1.2 in Table 2. The appearance band at 1394 cm^{-1} was referred to the -CH2 deformation vibration on the $CuMn_2O_4$ sample, which is often associated with carboxy (-CH_2-COOH). However, the -CH_2 vibration was not found in DRIFTS spectra of amorphous samples. The peaks at 2340 and 2361 cm^{-1} were attributed to the generation of CO_2, and the peak at 2189 cm^{-1} was assigned to CO. No obvious characteristic peaks of toluene were observed (at 3072 cm-1), it seems that the oxidation of toluene to the mentioned intermediates given above was faster than the adsorption of toluene.

In addition, the detection of $Cu_xMn_yO_zH_w^+$ secondary ions using TOF-SIMS has been depicted in Fig. S7. The CuOMn+ secondary signal contributes in relative intensity to 1.9%, 3.7%, and 1.6% in polarity (+) based on the total intensity of $CuMn_2O_4$, $Cu_{0.2}MnO_x$, $Cu_{0.3}MnO_x$, respectively. This indicates the better Mn-O-Cu interactions for $Cu_{0.2}MnO_x$. In addition, $C_7H_7^+$ (toluene) appeared as seen in Fig. 9, which was thought to be adsorbed firstly. $C_7OH_5^+$ (benzyl alcohol), $C_7OH_7^+$ (benzaldehyde), and $C_7O_2H_5^+$ (benzoic acid) were also revealed as the results of DRIFTS, and were considered to be intermediates in the decomposition of toluene to benzoic acid (Eq.1.3-1.6). In addition, some ions, such as $C_6H_5O^+$ and $C_7O_2H_7^+$ referred to phenol and O-methyl hydroquinone, were involved in the formation of p-toluquinone ($C_7O_2H_7^+$) in agreement with the previous discussion. Some other ring-breaking compounds such as maleic anhydride ($C_4O_3H^+$), acetic acid ($C_2H_3O_2^+$), and formic acid (HCO_2^+) were revealed, involving the formation of benzyl formate and benzyl acetate. In short, three possible toluene oxidation pathways were proposed based on the above analysis (Fig. 8). One is that toluene was oxidized for the formation of benzaldehyde, and then further oxidized to form benzoic acid. Hence, benzene could be formed through the decarboxylation process or demethylation of toluene. For ring-open reactions, the maleic anhydride, propanol, or other acids (acetic acid, formic acid) were generated as main intermediate products prior to the production of CO_2 or CO. No obvious diversity of byproducts among the three samples, but the intermediate products were oxidized in different reaction rate, leading to the diversity of carbon balance, which was in agreement with different intensity of IR bands in different samples.

3.4. The mechanism analysis of catalytic ozonation

The characteristics of post-experiment samples were analyzed, as seen in Fig. S8, no obvious phase change was observed. The morphologies of samples showed grain aggregation as seen in Fig. S9. This was also confirmed by pore diameter results in Table 1. Dp increased after the ozonation process. In addition, it was suggested that the carbon deposit may cause the change of SBET [39], the decrease of SBET was observed for all samples. Furthermore, TGA/DTG curves for samples are displayed in Fig. S10 and summarized in Table S4. It was observed that a total weight loss of 6.7, 15.8, and 23.7 wt% for $CuMn_2O_4$, $Cu_{0.2}MnO_x$, and $Cu_{0.3}MnO_x$, respectively. According to DTG curves, the weight losses from 30 to 300℃ were ascribed to water desorption (30-150℃) and chemically bonding water (150-300℃). The second weight loss of 1.4 wt%, 3.7 wt%, and 5.5 wt% at 300-600℃ was found for $CuMn_2O_4$, $Cu_{0.2}MnO_x$, and $Cu_{0.3}MnO_x$, respectively, suggesting the desorption of carbon deposits [40].

Commercial catalyst $Cu_{0.3}MnO_x$ showed the highest weight loss, suggesting the incomplete ozonation process.

The valence states of samples on the surface were characterized using XPS (Fig. S11). After ozonation reactions, the Cu^+ content of $CuMn_2O_4$ (27.5%) and Mn AOS (3.8) decreased to 13.1% and 3.6, respectively. The possible reaction was proposed: $\equiv Mn^{4+} + \equiv Cu^{2+} + 2O_{lat} \rightarrow \equiv Mn^{2+}/Mn^{3+} + Vo + \equiv Cu^+ + O_2$ [10], indicating that Cu-O (Cu^+/Cu^{2+}) exist as an electron mediator on the degradation of toluene, while, it may as an adsorption site, giving electrons for O_3 decomposition to form active O species, then, toluene was further oxidized on the site of Mn^{4+} as Fig. 10 shown. The bonding of Cu^+-O^{2-}-Mn^{4+} of the spinel structure, exhibiting highly oxidizing ability, transformed to the Cu^{2+}-O^{2-}-Mn^{3+} in the oxidation of toluene [41].

On the other hand, Mn AOS of $Cu_{0.2}MnO_x$ and $Cu_{0.3}MnO_x$ decreased from 3.5 and 3.8 to 3.0 and 3.6, respectively, indicating the reduction of Mn. It is worth noting that Cu-O (Cu^+/Cu^{2+}) generally participates in the reaction as an adsorption site [42], and the valence state of Cu was unchanged in the amorphous sample, indicating the main ozonation process occurred via Mn atom (Eq. 2.1-2.4). This may suggest the different ozonation processes between amorphous samples and spinel samples, i.e. the possible replenishment process of electrons on Cu^+/Cu^{2+} in amorphous samples. It was observed the ratio of O_{ads}/O_{lat} (Table 1) increased after reaction implied the consumption of O_{lat}, which was in agreement with the increase of O_v for amorphous samples. Therefore, the structural defects of amorphous cannot be ignored on the surface of samples. Hence, it is suggested the strong oxidizing group (O^-, O_2^-, O_2^{2-}) produced by the decomposition of O_3 could be captured by Vo due to the positive property of Vo, and then the adjacent adsorbed toluene was oxidized by reactive O to form the byproducts as discussed above.

All in all, according to the above analyses, the mechanism of catalytic ozonation of toluene could be proposed as presented in Fig. 10. At first, toluene was adsorbed into Cu^+/Cu^{2+} (Eq. 3.1-3.2). For amorphous samples, toluene was chemisorbed to be C_7H_7- by the electrons from charge-transfer of $Cu^+ \rightarrow Cu^{2+}$, the replenishment of $Cu^{2+} \rightarrow Cu^+$ occurred due to the formation of oxygen vacancies. These oxygen vacancies were thought to be generated from the process of $Mn^{4+} \rightarrow Mn^{2+}/Mn^{3+}$ in accompany with the decomposition of O_3, leading to the decrease of Mn AOS (Eq. 2.1-2.3). Hence, Mn was believed to be the most reactive site on the amorphous sample for catalytic ozonation. On the other hand, for $CuMn_2O_4$, the electrons from $Cu^{2+} + Mn^{2+}/Mn^{3+} \leftrightharpoons Cu^+ + Mn^{3+}/Mn^{4+}$ were used for ozonation process. Considering to generation of Vo during O3 decomposition, the chemical reaction equilibrium of Eq. 4.1 shifts to left, leading to a lower content of Cu^+/Mn^{4+}.

4. Conclusion

The catalytic activities of various Cu-Mn catalysts (spinel and amorphous) for the oxidation of toluene have been examined. Firstly, it is observed that the catalytic ozonation of toluene has higher efficiency (91.2%) and CO_x yield (83.0%) by using $Cu_{0.2}MnO_x$ at 130 min in comparison with other samples. Secondly, the chemisorption and catalytic capabilities of Cu-Mn catalysts can be attributed to the synergistic effects between Cu and Mn, such as the electron-transfer process. The well-dispersed Vo on the surface of amorphous catalysts helped the chemisorption of O_3, and adjacent Mn was believed to be as a main active site in the reaction. In addition, $CuMn_2O_4$ exhibited spinel crystal structure, adjunction sites of Cu^+/Mn^{4+} were considered to be reactive sites. The consumed redox pair inhibited toluene further abatement. At last, the possible routes of ozone-assisted catalytic oxidation toluene were proposed over Cu-Mn catalysts, the different physic-chemical properties of Cu-Mn catalysts result in different reaction rates of intermediates decomposition, leading to different amounts of byproducts and toluene abatement efficiency.

Acknowledgment

References
[1] C. Yang, G. Miao, Y. Pi, Q. Xia, J. Wu, Z. Li, J. Xiao, Abatement of various types of VOCs by adsorption/catalytic oxidation: A review, Chem. Eng. J., 370 (2019) 1128-1153.
[2] F. Lin, Z. Zhang, N. Li, B. Yan, C. He, Z. Hao, G. Chen, How to achieve complete elimination of Cl-VOCs: A critical review on byproducts formation and inhibition strategies during catalytic oxidation, Chem. Eng. J., 404 (2021) 126534.
Journal Pre-proof
20
[3] N. Li, Q. Jiang, F. Wang, J. Xie, Y. Li, J. Li, S. Wu, Emission behavior, environmental impact and priority-controlled pollutants assessment of volatile organic compounds (VOCs) during asphalt pavement construction based on laboratory experiment, J. Hazard. Mater., 398 (2020) 122904.
[4] H. Einaga, Y. Teraoka, A. Ogata, Catalytic oxidation of benzene by ozone over manganese oxides supported on USY zeolite, J. Catal., 305 (2013) 227-237.
[5] H.C. Wang, H.S. Liang, M.B. Chang, Chlorobenzene oxidation using ozone over iron oxide and manganese oxide catalysts, J. Hazard. Mater., 186 (2011) 1781-1787.
[6] H. Huang, X. Ye, W. Huang, J. Chen, Y. Xu, M. Wu, Q. Shao, Z. Peng, G. Ou, J. Shi, X. Feng, Q. Feng, H. Huang, P. Hu, D.Y.C. Leung, Ozone-catalytic oxidation of gaseous benzene over MnO2/ZSM-5 at ambient temperature: Catalytic deactivation and its suppression, Chem. Eng. J., 264 (2015) 24-31.
[7] D. Wang, H. Xu, J. Ma, X. Lu, J. Qi, S. Song, Strong promoted catalytic ozonation of atrazine at low temperature using tourmaline as catalyst: Influencing factors, reaction mechanisms and pathways,
Chem. Eng. J., 354 (2018) 113-125.
[8] M. Li, K.N. Hui, K.S. Hui, S.K. Lee, Y.R. Cho, H. Lee, W. Zhou, S. Cho, C.Y.H. Chao, Y. Li, Influence of modification method and transition metal type on the physicochemical properties of MCM-41 catalysts and their performances in the catalytic ozonation of toluene, Appl. Catal. B-Environ., 107 (2011) 245-252.
[9] S. Jo, K.T. Kim, D.H. Lee, Y.H. Song, J.O. Lee, T. Lee, H.S. Han, Low temperature activation of CO removal by O3-assisted catalysis, Environ. Sci. Technol., 48 (2014) 14543-14548.
[10] J. Yang, Y. Huang, Y.-W. Chen, D. Xia, C.-Y. Mou, L. Hu, J. Zeng, C. He, P.K. Wong, H.-Y. Zhu, Active site-directed tandem catalysis on CuO/VO-MnO2 for efficient and stable catalytic ozonation of S-VOCs under mild condition, Nano Today, 35 (2020) 100944.
[11] R. Yang, P. Han, Y. Fan, Z. Guo, Q. Zhao, Y. Wang, S. Che, S. Lin, R. Zhu, The performance and reaction pathway of δ-MnO2/USY for catalytic oxidation of toluene in the presence of ozone at room temperature, Chemosphere, 247 (2020) 125864.
[12] W. Hong, M. Shao, T. Zhu, H. Wang, Y. Sun, F. Shen, X. Li, To promote ozone catalytic decomposition by fabricating manganese vacancies in ε-MnO2 catalyst via selective dissolution of Mn-Li precursors, Appl. Catal. B-Environ., 274 (2020) 119088.
[13] M. Hu, K.S. Hui, K.N. Hui, Role of graphene in MnO2/graphene composite for catalytic ozonation of gaseous toluene, Chem. Eng. J., 254 (2014) 237-244.
[14] G. Chen, Z. Wang, F. Lin, Z. Zhang, H. Yu, B. Yan, Z. Wang, Comparative investigation on catalytic ozonation of VOCs in different types over supported MnOx catalysts, J. Hazard. Mater., 391 (2020) 122218.
[15] J. Liu, L. Ke, J. Liu, L. Sun, X. Yuan, Y. Li, D. Xia, Enhanced catalytic ozonation towards oxalic

acid degradation over novel copper doped manganese oxide octahedral molecular sieves nanorods, J.

Hazard. Mater., 371 (2019) 42-52.

[16] Y. Shu, M. He, J. Ji, H. Huang, S. Liu, D.Y.C. Leung, Synergetic degradation of VOCs by vacuum ultraviolet photolysis and catalytic ozonation over Mn-xCe/ZSM-5, J. Hazard. Mater., 364 (2019) 770-779.

[17] E. Rezaei, J. Soltan, N. Chen, Catalytic oxidation of toluene by ozone over alumina supported manganese oxides: Effect of catalyst loading, Appl. Catal. B-Environ., 136-137 (2013) 239-247.

[18] W. Yang, Z.a. Su, Z. Xu, W. Yang, Y. Peng, J. Li, Comparative study of α-, β-, γ- and δ-MnO2 on toluene oxidation: Oxygen vacancies and reaction intermediates, Appl. Catal. B-Environ., 260 (2020) 118150.

[19] F. Wang, H. Dai, J. Deng, G. Bai, K. Ji, Y. Liu, Manganese Oxides with Rod-, Wire-, Tube-, and Flower-Like Morphologies: Highly Effective Catalysts for the Removal of Toluene, Environ. Sci. Technol., 46 (2012) 4034-4041.

[20] Z. Ye, J.M. Giraudon, N. Nuns, P. Simon, N. De Geyter, R. Morent, J.F. Lamonier, Influence of the preparation method on the activity of copper-manganese oxides for toluene total oxidation, Appl. Catal.

B-Environ., 223 (2017) 154-166.

[21] R. Sun, J. Gao, G. Wu, P. Liu, W. Guo, H. Zhou, J. Ge, Y. Hu, Z. Xue, H. Li, P. Cui, X. Zheng, Y. Wu, G. Zhang, X. Hong, Amorphous metal oxide nanosheets featuring reversible structure transformations as sodium-ion battery anodes, Cell Rep. Phys. Sci., 1 (2020) 100118.

[22] C.-W. Ahn, Y.-W. You, I. Heo, J.S. Hong, J.-K. Jeon, Y.-D. Ko, Y. Kim, H. Park, J.-K. Suh, Catalytic combustion of volatile organic compound over spherical-shaped copper-manganese oxide, J.

Ind. Eng. Chem., 47 (2017) 439-445.

[23] H. Chen, X. Tong, Y. Li, Mesoporous Cu-Mn Hopcalite catalyst and its performance in low temperature ethylene combustion in a carbon dioxide stream, Appl. Catal. A-Gen., 370 (2009) 59-65.

[24] Y. Wang, D. Yang, S. Li, L. Zhang, G. Zheng, L. Guo, Layered copper manganese oxide for the efficient catalytic CO and VOCs oxidation, Chem. Eng. J., 357 (2019) 258-268.

[25] J. Zhao, V. Malgras, J. Na, R. Liang, Y. Cai, Y. Kang, A.A. Alshehri, K.A. Alzahrani, Y.G. Alghamdi, T. Asahi, D. Zhang, B. Jiang, H. Li, Y. Yamauchi, Magnetically induced synthesis of mesoporous amorphous CoB nanochains for efficient selective hydrogenation of cinnamaldehyde to cinnamyl alcohol, Chem. Eng. J., 398 (2020) 125564.

[26] N. Huang, Z. Qu, C. Dong, Y. Qin, X. Duan, Superior performance of α@β-MnO2 for the toluene oxidation: Active interface and oxygen vacancy, Appl. Catal. A-Gen., 560 (2018) 195-205.

Journal Pre-proof

22

[27] T. Shen, W. Su, Q. Yang, J. Ni, S. Tong, Synergetic mechanism for basic and acid sites of MgMxOy (M = Fe, Mn) double oxides in catalytic ozonation of p-hydroxybenzoic acid and acetic acid, Appl. Catal. B-Environ., 279 (2020) 119346.

[28] Y. Xie, S. Peng, Y. Feng, D. Wu, Enhanced mineralization of oxalate by highly active and Stable Ce(III)-Doped g-C3N4 catalyzed ozonation, Chemosphere, 239 (2020) 124612.

[29] S. Yang, H. Yang, J. Yang, H. Qi, J. Kong, Z. Bo, X. Li, J. Yan, K. Cen, X. Tu, Three-dimensional hollow urchin α-MnO2 for enhanced catalytic activity towards toluene decomposition in post-plasma catalysis, Chem. Eng. J., 402 (2020) 126154.

[30] Z. Ye, Z. Ye, A. Nikiforov, J. Chen, W. Zhou, J. Chen, G. Wang, Y. Zhang, Influence of mixed-phase TiO2 on the activity of adsorption-plasma photocatalysis for total oxidation of toluene, Chem. Eng. J., (2020) 126280.

[31] S. Dissanayake, N. Wasalathanthri, A. Shirazi Amin, J. He, S. Poges, D. Rathnayake, S.L. Suib, Mesoporous Co3O4 catalysts for VOC elimination: Oxidation of 2-propanol, Appl. Catal. A-Gen., 590 (2020) 117366.

[32] J. Wang, W. Wang, J. Wang, K. Xue, Y. Peng, Y. Yan, Y. Wang, H. Wang, Y. Wu, The generation of

lattice oxygen defects enhanced by β particles: Layered microsphere-like Bi2WO6 as a template leads to Bix@Bi2-xWOn for the efficient removal of oxytetracycline, Chem. Eng. J., 416 (2021) 129197.

[33] F. Lin, Z. Wang, Z. Zhang, L. Xiang, D. Yuan, B. Yan, Z. Wang, G. Chen, Comparative investigation on chlorobenzene oxidation by oxygen and ozone over a MnOx/Al2O3 catalyst in the presence of SO2, Environ. Sci. Technol., 55 (2021) 3341-3351.

[34] J. Li, K. Li, B. Lei, M. Ran, Y. Sun, Y. Zhang, K.-H. Kim, F. Dong, High-efficiency photocatalytic decomposition of toluene over defective InOOH: Promotive role of oxygen vacancies in ring opening process, Chem. Eng. J., (2020) 127389.

[35] Z. Xiao, J. Yang, R. Ren, J. Li, N. Wang, W. Chu, Facile synthesis of homogeneous hollow microsphere Cu-Mn based catalysts for catalytic oxidation of toluene, Chemosphere, 247 (2020) 125812.

[36] J. Kim, J.E. Lee, H.W. Lee, J.K. Jeon, J. Song, S.C. Jung, Y.F. Tsang, Y.K. Park, Catalytic ozonation of toluene using Mn-M bimetallic HZSM-5 (M: Fe, Cu, Ru, Ag) catalysts at room temperature, J. Hazard. Mater., 397 (2020) 122577.

[37] J. Li, H. Na, X. Zeng, T. Zhu, Z. Liu, In situ DRIFTS investigation for the oxidation of toluene by ozone over Mn/HZSM-5, Ag/HZSM-5 and Mn-Ag/HZSM-5 catalysts, Appl. Surf. Sci., 311 (2014) 690-696.

[38] J. Schnaidt, M. Heinen, Z. Jusys, R.J. Behm, Oxidation of 1-propanol on a Pt film electrode studied by combined electrochemical, in situ IR spectroscopy and online mass spectrometry measurements, Electrochim. Acta, 104 (2013) 505-517.Journal Pre-proof
23

[39] B. Wang, C. Chi, M. Xu, C. Wang, D. Meng, Plasma-catalytic removal of toluene over CeO2-MnOx catalysts in an atmosphere dielectric barrier discharge, Chem. Eng. J., 322 (2017) 679-692.

[40] Z. Ye, J.-M. Giraudon, N. Nuns, G. Abdallah, A. Addad, R. Morent, N. De Geyter, J.-F. Lamonier, Preferential dissolution of copper from Cu-Mn oxides in strong acid medium: Effect of the starting binary oxide to get new efficient copper doped MnO2 catalysts in toluene oxidation, Appl. Surf. Sci., 537 (2021) 147993.

[41] S. Dey, V.V. Praveen Kumar, The performance of highly active manganese oxide catalysts for Ambient conditions carbon monoxide oxidation, Curr. Res. Green Sustain. Chem., 3 (2020) 100012.

[42] S. Xiong, N. Huang, Y. Peng, J. Chen, J. Li, Balance of activation and ring-breaking for toluene oxidation over CuO-MnO bimetallic oxides, J. Hazard. Mater., 415 (2021) 125637.

Figures:
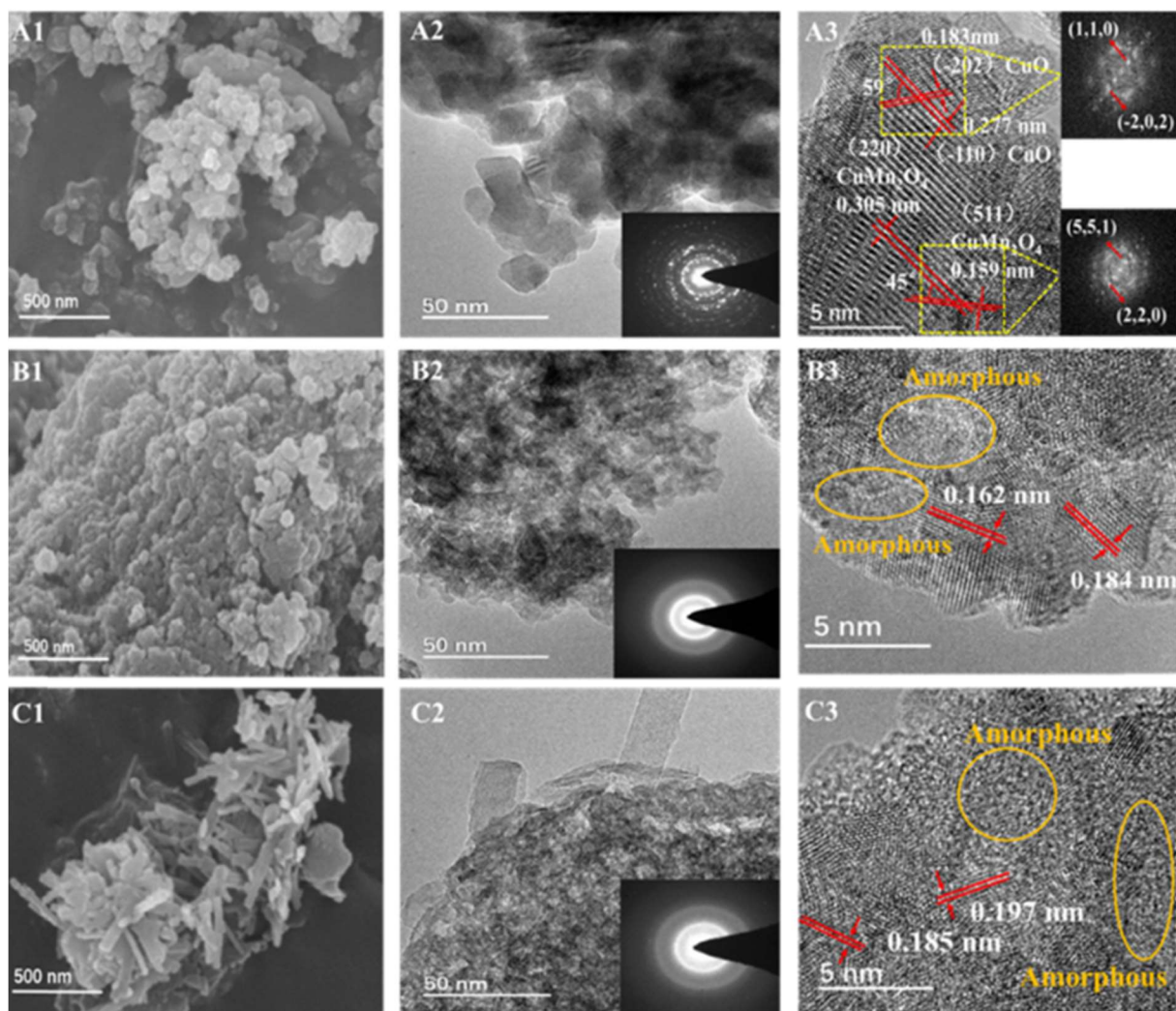
Fig. 1. SEM images of various Cu-Mn samples of $CuMn_2O_4$ (A1), $Cu_{0.2}MnO_x$ (B1), and $Cu_{0.3}MnO_x$ (C1) catalysts; HRTEM images of $CuMn_2O_4$ (A2-3), $Cu_{0.2}MnO_x$ (B2-3), and $Cu_{0.3}MnO_x$ (C2-3) catalysts.
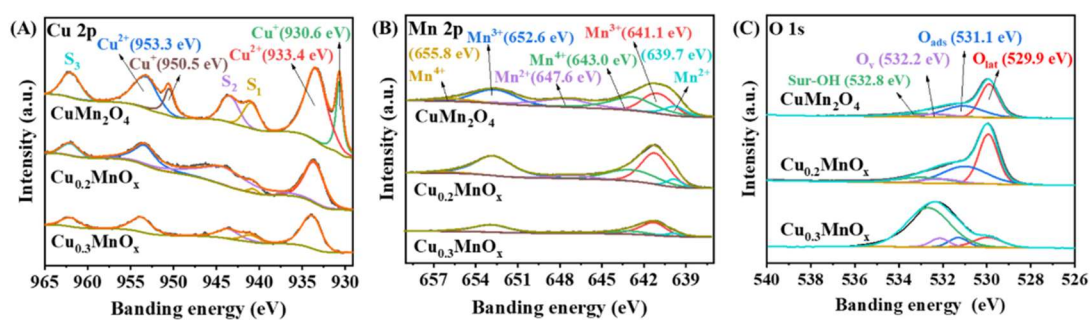
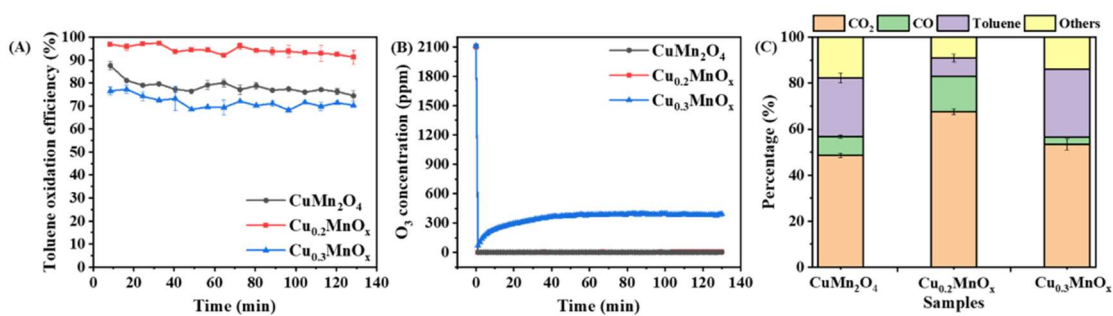Fig. 2. XPS spectra of $CuMn_2O_4$, $Cu_{0.2}MnO_x$, and $Cu_{0.3}MnO_x$. (A) Cu 2p, (B) Mn 2p, (C) O 1s.

Fig. 3. Toluene abatements on various samples at 100°C, ~160 ppm toluene, and ~2100 ppm O_3. (A)Toluene removal, (B) O3 residual, (C) Carbon balance at 130 min.
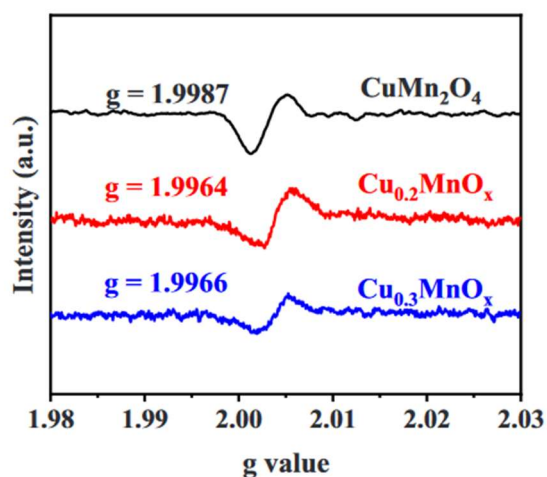
Fig. 4. EPR spectra of various samples
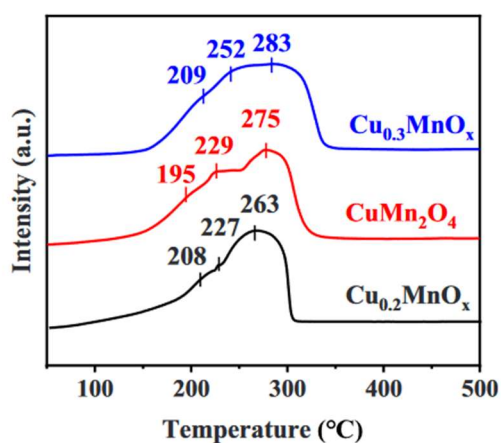
Fig. 5. H_2-TPR profiles of various samples.
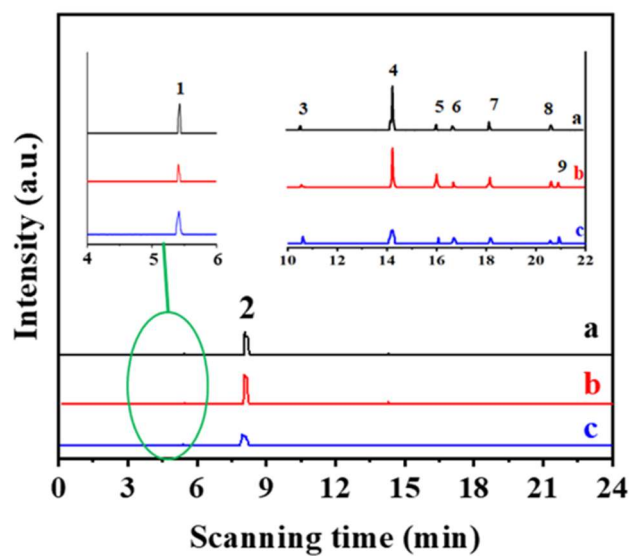
Fig. 6. GC-MS spectra of gaseous by-products by using various samples in the ozone-catalysis system (Lines a-c in order: $CuMn_2O_4$, $Cu_{0.2}MnO_x$, $Cu_{0.3}MnO_x$): (1) Propanol, (2) Toluene, (3) Maleic anhydride, (4) Benzaldehyde, (5) O-methyl benzoquinone, (6) Benzyl alcohol, (7) Benzyl formate, (8) Benzoic acid, (9) Benzyl acetate.
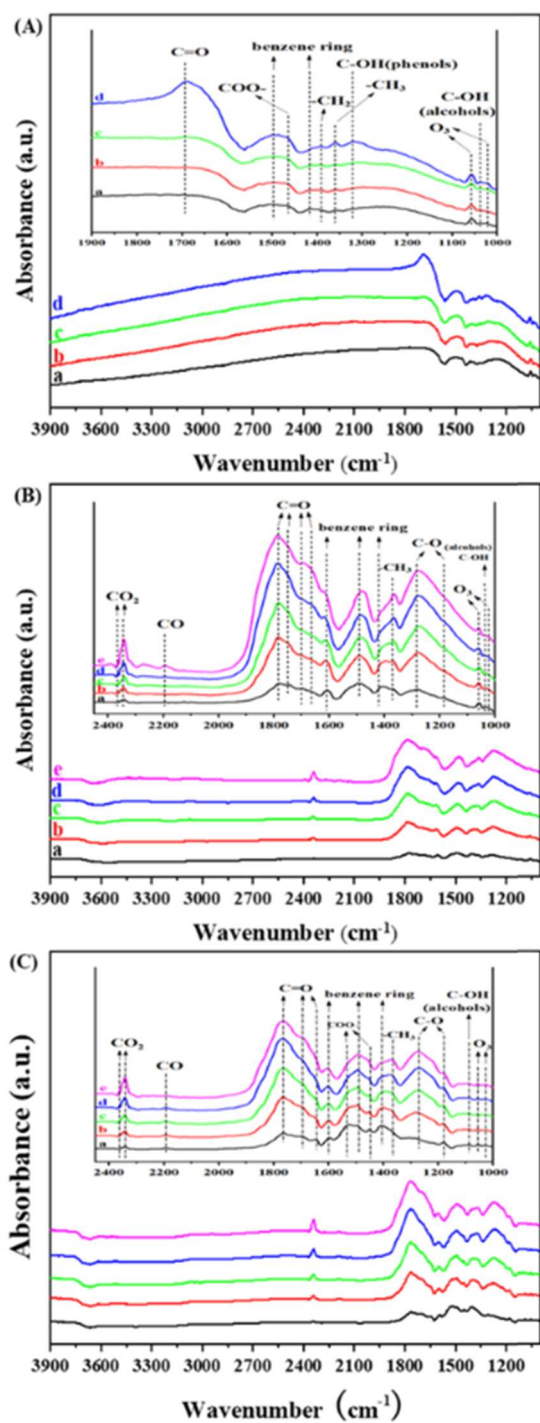
Fig. 7. DRIFTS of the substances on the surface of samples at 100°C and 2100 ppm O_3. (A) $CuMn_2O_4$ (Lines a-d in order: 1 min, 5 min, 16 min, 130 min), (B) Cu0.2MnOx (Lines a-e in order: 1 min, 3 min, 5 min, 16 min, 130 min), (C) $Cu_{0.3}MnO_x$ (Lines a-d in order: 1 min, 3 min, 5 min, 16 min, 130 min).
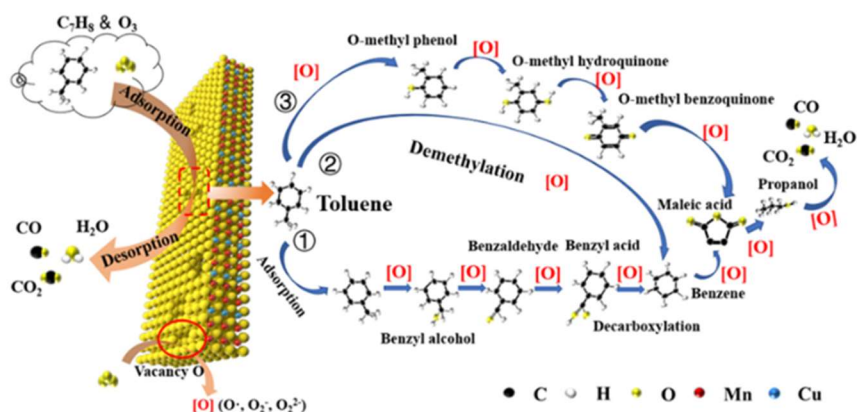
Fig. 8. The proposal reaction pathway over Cu-Mn catalyst for toluene oxidation with the presence of O_3.
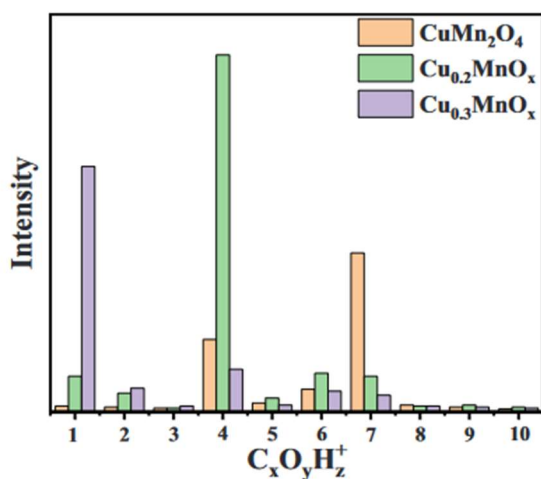
Fig. 9. The $C_xO_yH_z$ ions in polarity (+) for three samples: (1) HCO_2^+, (2) $C_3H_7O^+$, (3) $C_4O_3H^+$, (4) $C_6H_5^+$, (5) $C_6H_5O^+$, (6) $C_7H_7^+$, (7) $C_7OH_5^+$, (8) $C_7OH_7^+$, (9) $C_7O_2H_5^+$, (10) $C_7O_2H_7^+$.
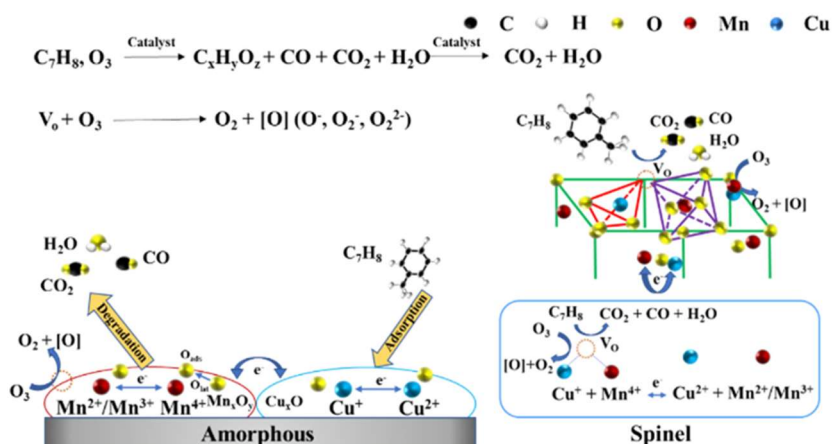
Fig. 10. The mechanisms of Cu-Mn bimetallic sites synergetic ozone-catalyzed oxidation of toluene.

Table 1 The relevant data about fresh and post reaction catalysts.

Table 1
The relevant data about fresh and post reaction catalysts.

Samples		S_{BET}^{a} (m²/g)	V_p^{b} (cm³/g)	D_p^{c} (nm)	O_{ads}/O_{lat}^{d}	$Cu^+/(Cu^++Cu^{2+})^{d}$	$Cu^{2+}/(Cu^++Cu^{2+})^{d}$	AOS_{Mn}^{d}	Cu/Mn^{e}	Cu/Mn^{f}	H_2-TPR^{g} (°C)
Fresh	$CuMn_2O_4$	61.4	0.1	4.7	0.7	27.5	72.5	3.6	0.5	0.5	275
	$CuMn_{0.2}O_x$	154.3	0.5	5.6	0.8	–	100	3.5	0.2	0.6	263
	$CuMn_{0.3}O_x$	156.3	0.2	2.3	0.6	–	100	3.8	0.3	2.1	283
Post-reaction	$CuMn_2O_4$	30.1	0.1	14.8	0.7	13.1	86.9	3.2			
	$CuMn_{0.2}O_x$	105.0	0.3	10.1	1.0	–	100	3.0			
	$CuMn_{0.3}O_x$	129.0	0.2	5.5	0.8	–	100	3.6			

[a] Surface Area.
[b] Desorption cumulative volume of pores.
[c] Desorption average pore diameter.
[d] From XPS results.
[e] Cu/Mn of the entire catalyst obtained from ICP-OES results
[f] Cu/Mn of the entire catalyst obtained from EDX results.
[g] The maximum temperature of reduction.

Table 2: Possible reactions for ozone catalytic oxidation process.

Catalytic ozonation process	
$CH_3CH_2CH_2\text{-}OH + O_{lat} \rightarrow CH_3CH_2CHO$	Eq. 1.1
$CH_3CH_2CHO + O_{lat} \rightarrow CH_3CH_2COOH$	Eq. 1.2
$C_6H_5\text{-}CH_3 + Ov \rightarrow C_6H_5\text{-}CH_3\text{-}O_v$	Eq. 1.3
$C_6H_5\text{-}CH_3\text{-}Ov + O_{lat} \rightarrow C_6H_5\text{-}CH_2OH$	Eq. 1.4
$C_6H_5\text{-}CH_2OH + O_{lat} \rightarrow C_6H_5\text{-}CHO + H_2O$	Eq. 1.5
$C_6H_5\text{-}CHO + O_{lat} \rightarrow C_6H_5\text{-}COOH$	Eq. 1.6
Mn element reaction process	
$Mn^{2+}/Mn^{3+} + O_3 + O_v \rightarrow O_2 + O_2^{2-}{}_{ads} + Mn^{3+}/Mn^{4+}$	Eq. 2.1
$O_2^{2-}{}_{ads} + Mn^{3+}/Mn^{4+} \rightarrow Mn^{3+}/Mn^{4+} + O^{2-} + O_{ads}$	Eq. 2.2
$Mn^{3+}/Mn^{4+} + O_{lat} \rightarrow Mn^{2+}/Mn^{3+} + O_2 + O_v$	Eq. 2.3
$C_7H_8 + Mn^{3+}/Mn^{4+} + O_{ads}/O_{lat} \rightarrow H_2O + CO_2 + Mn^{2+}/Mn^{3+} + Ov$	Eq. 2.4
Toluene chemisorption	
$Cu^+ + C_7H_8 \rightarrow C_7H_7\text{-}Cu + H^+$	Eq. 3.1
$Cu^+ + 2\ C_7H_8 \rightarrow C_7H_7\text{-}Cu\text{-}C_7H_7 + 2\ H^+$	Eq. 3.2
Charge transfer process	
$Cu^{2+} + Mn^{2+}/Mn^{3+} \leftrightarrows Cu^+ + Mn^{3+}/Mn^{4+}$	Eq. 4.1
$Cu^+ + Mn^{4+}/Mn^{3+} \leftrightarrows Mn^{2+}/Mn^{3+} + Cu^{2+}$	Eq.4.2

Supporting Information

Investigation of Cu-Mn catalytic ozonation of toluene: Crystal phase, intermediates and mechanism

Zhiping Ye,[a] Guanjie Wang,[a] Jean-marc giraudon,[b] Anton Nikiforov,[c] Jun Chen,[d] Liang Zhao,[a] Xiuwen Zhang,[a] Jiade Wang [a,]*

[a] College of Environmental, Zhejiang University of Technology, 18 Chaowang RD, Xiacheng District, Hangzhou, China

[b] Univ. Lille, CNRS, Centrale Lille, ENSCL, Univ. Artois, UMR 8181 - UCSS - Unite de Catalyse et Chimie du Solide, F-5900 Lille, France

[c] Ghent University, Faculty of Engineering, Department of Applied Physics, Research Unit Plasma Technology, Sint-Pietersnieuwstraat 41, 9000 Ghent, Belgium

[d] Interdisciplinary Research Academy, Zhejiang Shuren University, Hangzhou, 310021, P.R. China

*Corresponding author

E-mail: jdwang@zjut.edu.cn

This Supporting Information provides:
Total number of pages: 12
Total number of Figures: 11
Total number of Tables: 4
Text
1. Relevant calculation
Figure and Table
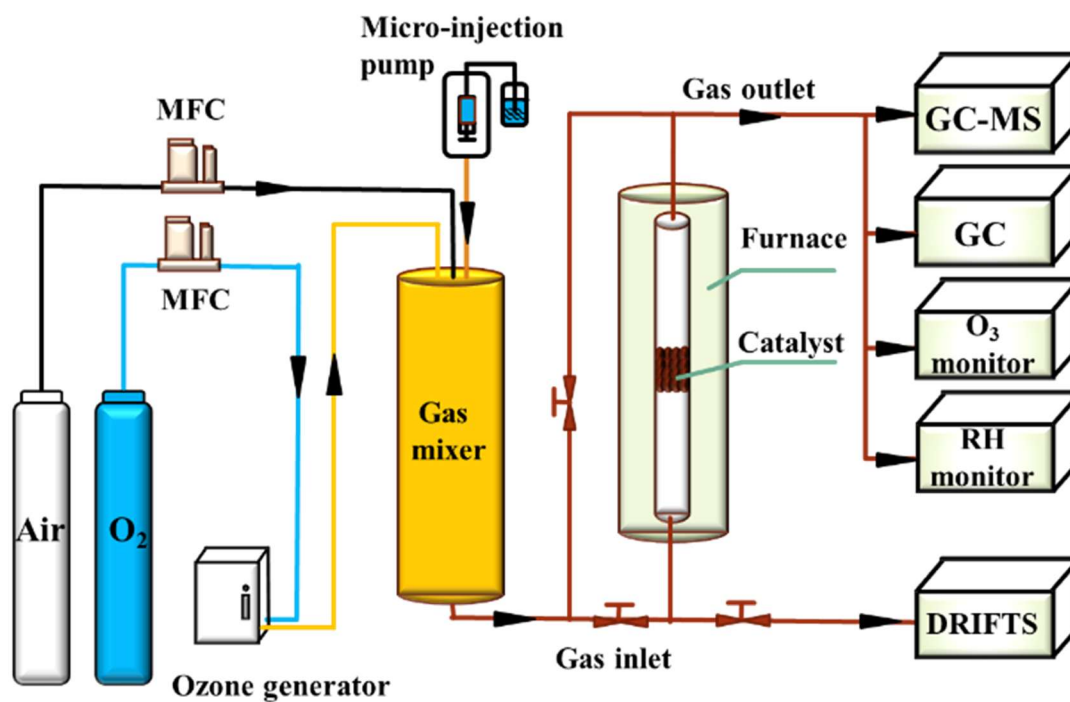Fig. S1. Schematic diagram of catalyst activity testing device.
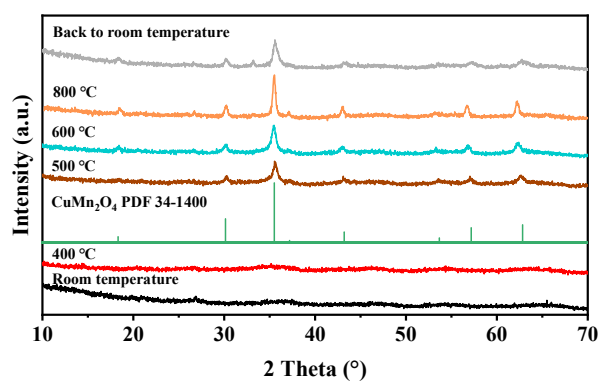Fig. S2. Powder XRD patterns of $CuMn_2O_4$, $Cu_{0.2}MnO_x$, and $Cu_{0.3}MnO_x$.
Fig. S3. In situ XRD patterns of $Cu_{0.3}MnO_x$ under flowing N_2 as a function of temperature.
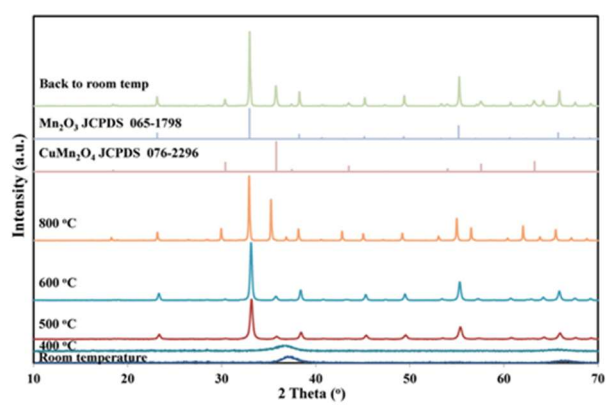Fig. S4. In situ XRD patterns of $Cu_{0.2}MnO_x$ under flowing N2 as a function of temperature.
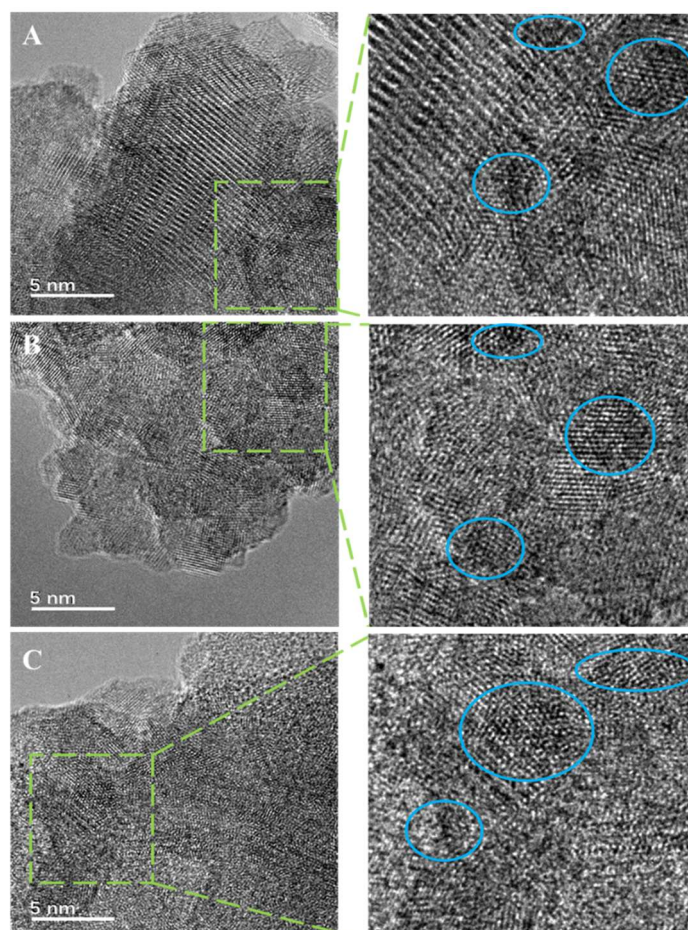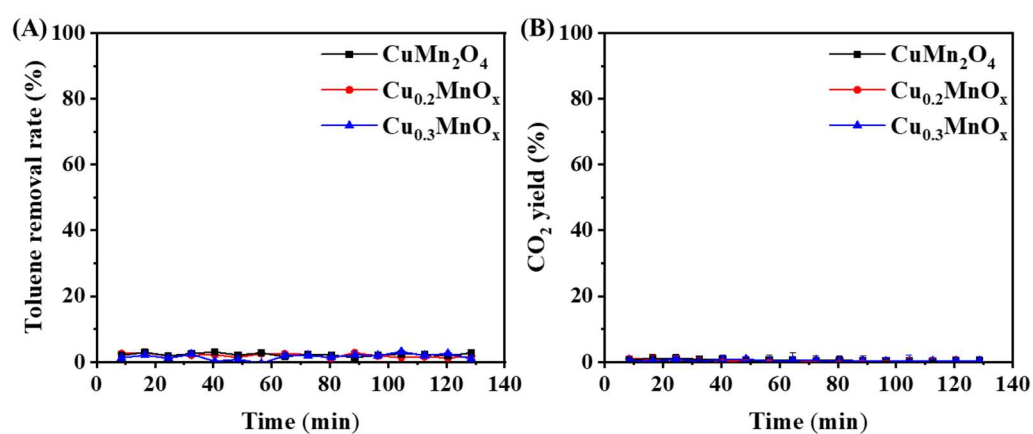Fig. S5 HRTEM images of $CuMn_2O_4$ (A), $Cu_{0.2}MnO_x$ (B), and $Cu_{0.3}MnO_x$ (C) catalysts.
Fig. S6. Toluene abatements on various samples without O_3. (A) Toluene removal rate, (B) CO_2 yield.
Fig. S7. The $Cu_xMn_yO_zH_w$ ions in polarity (+) for three samples: (1) MnCuO, (2) $^{65}CuMnO$, (3) CuMnOH, (4) $^{65}CuMnOH$, (5) CuMn, (6) CuMnH, (7) $CuMnO_2$, (8) $CuMnO_2H^+$, (9) $CuMnO_2H_2$, (10) $^{65}CuMnO_2H$, (11) $^{65}CuMnO_2H_2$, (12) $CuMn_2O_2$, (13) $^{65}CuMn_2O_2$, (14) $CuMn_2O_3$, (15) $^{65}CuMn_2O_3$, (16) $CuMn_2O_3H$, (17) $^{65}CuMn_2O_3H$, (18) $CuMn_3O_3$, (19) $^{65}CuMn_3O_3$, (20) $CuMn_3O_4$, (21) $^{65}CuMn_3O_4$.
Fig. S8. Powder XRD patterns of the post-reaction various Cu-Mn samples.
Fig. S9. SEM images of the post-reaction Cu-Mn samples. (A) $CuMn_2O_4$, (B) $Cu_{0.2}MnO_x$, (C) $Cu_{0.3}MnO_x$.
Fig. S10. TGA/DTG analyses of the post-reaction catalysts.
Fig. S11. XPS spectra of the post-reaction various Cu-Mn samples. (A) Cu 2p, (B) Mn 2p, (C) O 1s.

Table S1 Catalytic ozonation of toluene by various samples.
Table S2 Attribution of main characteristic peaks in DRIFTS.
Table S3 Main by-products in the exhaust gas.
Table S4 TG of various samples.

1. Relevant calculation

Toluene removal rate (TRR), CO yield (X_{CO}) and CO_2 yield (X_{CO2}), and others (X_O) were calculated as follows:

$$TPR\ (\%) = \frac{[Toluene]_{inlet} - [Toluene]_{outlet}}{[Toluene]_{inlet}} \times 100\% \qquad (1)$$

$$X_{CO}\ (\%) = \frac{[CO]}{[Toluene]_{inle} \times 7} \times 100\% \qquad (2)$$

$$X_{CO_2}\ (\%) = \frac{[CO_2]}{[Toluene]_{inlet} \times 7} \times 100\% \qquad (3)$$

$$X_O\ (\%) = (1 - X_{CO} - X_{CO_2} - TPR) \times 100\% \qquad (4)$$

Here, $[Toluene]_{inlet}$ is toluene concentration (ppm) in the mixture at the inlet, $[Toluene]_{outlet}$ is toluene concentration (ppm) in the mixture at the outlet. $[CO]$ and $[CO_2]$ are the concentration of CO_2 and CO (ppm) in the gas stream outlet during the oxidation reaction, respectively.

Fig. S1. Schematic diagram of catalyst activity testing device.
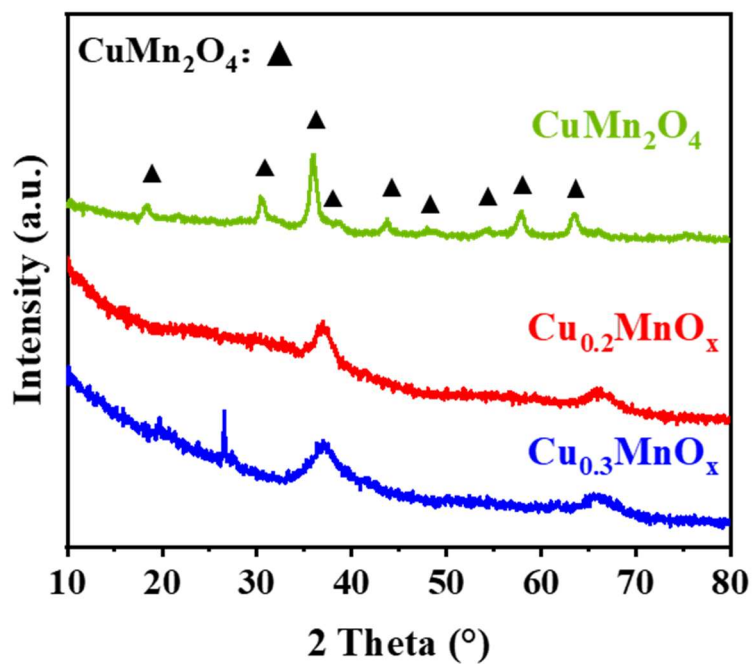
Fig. S2. Powder XRD patterns of fresh samples of $CuMn_2O_4$, $Cu_{0.2}MnO_x$, and $Cu_{0.3}MnO_x$.

Fig. S3. In situ XRD patterns of $Cu_{0.3}MnO_x$ under flowing N_2 as a function of temperature.

Fig. S4. In situ XRD patterns of $Cu_{0.2}MnO_x$ under flowing N_2 as a function of temperature.

Fig. S5. HRTEM images of $CuMn_2O_4$ (A), $Cu_{0.2}MnO_x$ (B), and $Cu_{0.3}MnO_x$ (C) catalysts.

Fig. S6. Toluene abatements on various samples without O_3. (A) Toluene removal rate, (B) CO_2 yield.

Fig. S7. The $Cu_xMn_yO_zH_w$ ions in polarity (+) for three samples: (1) MnCuO, (2) ^{65}CuMnO, (3) CuMnOH, (4) ^{65}CuMnOH, (5) CuMn, (6) CuMnH, (7) $CuMnO_2$, (8) $CuMnO_2H^+$, (9) $CuMnO_2H_2$, (10) ^{65}CuMnO_2H, (11) ^{65}CuMnO_2H_2, (12) $CuMn_2O_2$, (13) ^{65}CuMn_2O_2, (14) $CuMn_2O_3$, (15) ^{65}CuMn_2O_3, (16) $CuMn_2O_3H$, (17) ^{65}CuMn_2O_3H, (18) $CuMn_3O_3$, (19) ^{65}CuMn_3O_3, (20) $CuMn_3O_4$, (21) ^{65}CuMn_3O_4.

Fig. S8. Powder XRD patterns of the post-reaction various Cu-Mn samples.

Fig. S9. SEM images of the post-reaction Cu-Mn samples. (A) $CuMn_2O_4$, (B) $Cu_{0.2}MnO_x$, (C) $Cu_{0.3}MnO_x$.
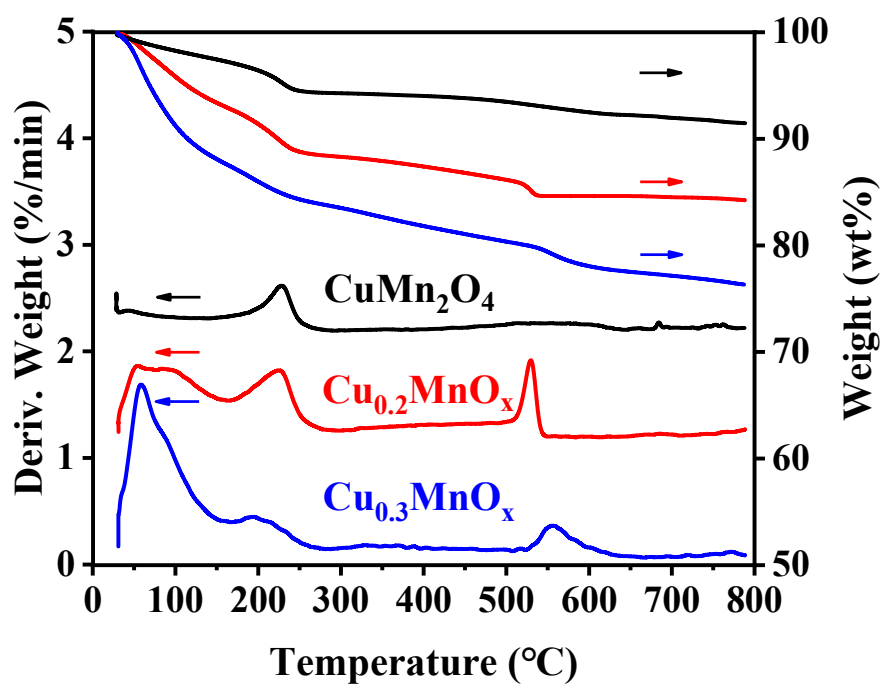
Fig. S10. TGA/DTG analyses of the post-reaction catalysts.
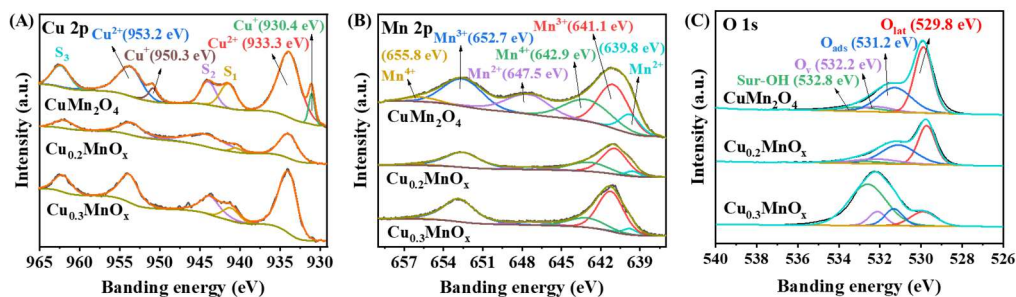

Fig. S11. XPS spectra of the post-reaction various Cu-Mn samples. (A) Cu 2p, (B) Mn 2p, (C) O 1s.

Table S1 Catalytic ozonation of toluene by various samples.

Samples	Metal loading (wt%)	Temperature (°C)	O_3 (ppm)	Toluene (ppm)	Reaction time (min)	Toluene removal (%)	O_3 removal (%)	Ref.
Cu (imp)/MCM-41	4	22	1345	395	88	33	38	[1]
Cu (insitu)/MCM-41	4	22	1345	395	88	15	36	[1]
δ-MnO_2/USY	3	25	60	20	180	55	100	[2]
Cu-Mn/HZSM-5	1(Cu), 5(Mn)	25	1000	100	-	27	27	[3]
Ru-Mn/HY (80)	1(Ru), 5(Mn)	25	1000	100	-	63	89	[4]
Cu/13X	2	90	7650	896	100	15	24	[5]
Mn/13X	2	90	7650	896	100	47	63	[5]
MnO_x/γ-Al_2O_3	5	120	1000	100	150	100	100	[6]
$Cu_{0.2}MnO_x$	-	100	2100	160	130	91	100	
$CuMn_2O_4$	-	100	2100	160	130	75	100	
$Cu_{0.3}MnO_x$	-	100	2100	160	130	70	80	

Table S2 Attribution of main characteristic peaks in DRIFTS.

Wavenumber (cm^{-1})	Ascription	Characteristic substances
1026, 1056, 2122		O_3
1039	C-OH stretching vibration	Alcohols
1180, 1275	C-O stretching vibration	Alcohols or phenols
1309	C-OH Vibration peak	Phenols
1368	-CH_3 Vibration peak	Methyl
1394	-CH_2 Vibration peak	Methylene
1410, 1498, 1600	C=C Vibration peak	Benzene ring
1450, 1555	COO- stretching vibration	Acids
1656, 1696, 1755, 1785	C=O stretching vibration	Quinone, aldehydes, acids or esters
2195	CO	CO
2340, 2361	CO_2	CO_2
3072	C-H aromatic ring	Toluene

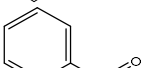Table S3 Main by-products in the exhaust gas.
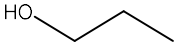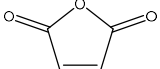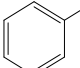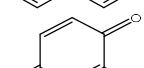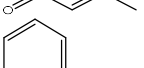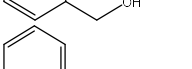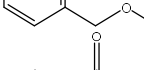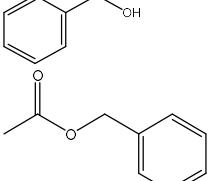
Number	Peak time (min)	Chemical compound	Molecular formula	Structural formula
Ring-opening organic compound	5.414	Propanol	C_3H_8O	
	10.591	Maleic anhydride	$C_4H_2O_3$	
Benzenoids	8.005	Toluene	C_7H_8	
	14.255	Benzaldehyde	C_7H_6O	
	16.031	O-methylbenzoquinone	$C_7H_6O_2$	
	16.709	Benzyl alcohol	C_7H_8O	
	18.18	Benzyl formate	$C_8H_8O_2$	
	20.646	Benzoic acid	$C_7H_6O_2$	
	20.925	Benzyl acetate	$C_9H_{10}O_2$	

Table S4 TG of various samples.

Samples	30-300°C (%)	300-600°C (%)	600-790°C (%)	30-790°C (%)
$CuMn_2O_4$	4.5	1.4	0.8	6.7
$Cu_{0.2}MnO_x$	11.7	3.7	0.4	15.8
$Cu_{0.3}MnO_x$	16.5	5.5	1.7	23.7

Reference

[1] M. Li, K.N. Hui, K.S. Hui, S.K. Lee, Y.R. Cho, H. Lee, W. Zhou, S. Cho, C.Y.H. Chao, Y. Li, Influence of modification method and transition metal type on the physicochemical properties of MCM-41 catalysts and their performances in the catalytic ozonation of toluene, Appl. Catal. B-Environ. 107 (3-4) (2011) 245-252. https://doi.org/10.1016/j.apcatb.2011.07.018.

[2] R. Yang, P. Han, Y. Fan, Z. Guo, Q. Zhao, Y. Wang, S. Che, S. Lin, R. Zhu, The performance and reaction pathway of δ-MnO$_2$/USY for catalytic oxidation of toluene in the presence of ozone at room temperature, Chemosphere 247 (2020) 125864. https://doi.org/10.1016/j.chemosphere.2020.125864.

[3] J. Kim, J.E. Lee, H.W. Lee, J.K. Jeon, J. Song, S.C. Jung, Y.F. Tsang, Y.K. Park, Catalytic ozonation of toluene using Mn-M bimetallic HZSM-5 (M: Fe, Cu, Ru, Ag) catalysts at room temperature, J. Hazard. Mater. 397 (2020) 122577. https://doi.org/10.1016/j.jhazmat.2020.122577.

[4] J. Kim, E.E. Kwon, J.E. Lee, S.H. Jang, J.K. Jeon, J. Song, Y.K. Park, Effect of zeolite acidity and structure on ozone oxidation of toluene using Ru-Mn loaded zeolites at ambient temperature, J. Hazard. Mater. 403 (2021) 123934. https://doi.org/10.1016/j.jhazmat.2020.123934.

[5] T. Gopi, G. Swetha, S.C. Shekar, R. Krishna, C. Ramakrishna, B. Saini, P.V.L. Rao, Ozone catalytic oxidation of toluene over 13X zeolite supported metal oxides and the effect of moisture on the catalytic process, Arab. J. Chem. 12 (8) (2019) 4502-4513. https://doi.org/10.1016/j.arabjc.2016.07.018.

[6] J. Shao, F. Lin, Z. Wang, P. Liu, H. Tang, Y. He, K. Cen, Low temperature catalytic ozonation of toluene in flue gas over Mn-based catalysts: Effect of support property and SO$_2$/water vapor addition, Appl. Catal. B-Environ. 266 (2020) 118662. https://doi.org/10.1016/j.apcatb.2020.118662.

CrediT authorship contribution statement

Zhiping Ye: validation, results analysis, methodology, and writing; Guanjie Wang: Test experiment, results analysis, methodology, and writing; Jean-marc Giraudon: Conceptualization, validation, writing-review and editing, Anton Nikiforov: Conceptualization, validation, writing-review and editing, Jun Chen: Conceptualization, validation, writing-review and editing; Liang Zhao: Catalyst characterization; Xiuwen Zhang: Catalyst characterization; Jiade Wang: Funding support, supervision, validation.

Declaration of Competing Interest

The authors declare that they have no known competing financial interests or personal relationships that could have appeared to influence the work reported in this paper.

Graphical abstract
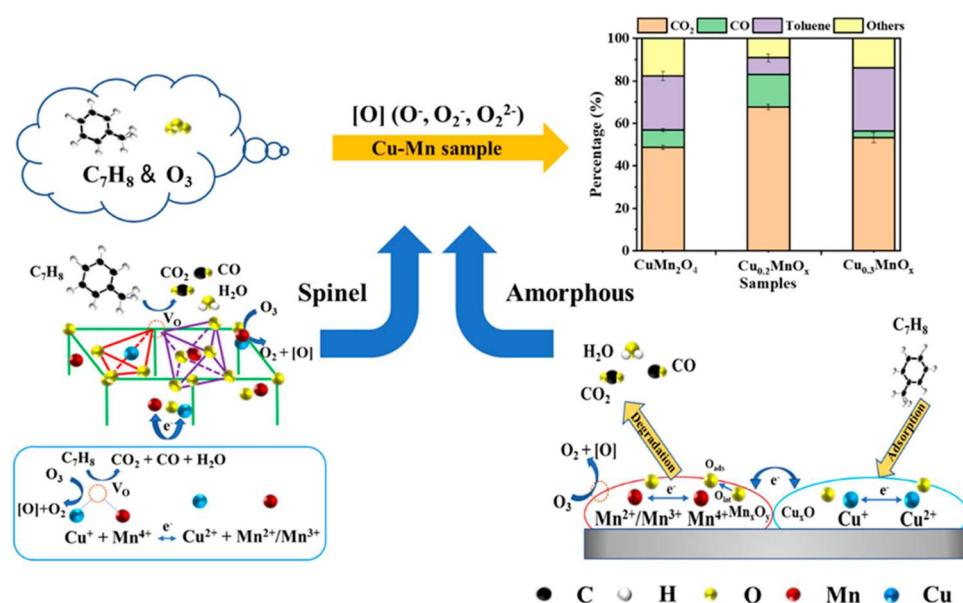
Highlights

- Amorphous phase of Cu-Mn oxides is more active than spinel
phase of sample in catalytic ozonation of toluene.
- High dispersion of Mn and oxygen vacancy played important role
for amorphous samples in catalytic ozonation process.
- Redox pair of $Cu^{+/2+}/Mn^{4+/3+}$ in spinel acted as active site for

degradation of ozone and toluene.
- No obvious difference was observed in the distribution of byproducts, except for the quantities.